




Dynamics of local photoconductivity in GaAs and InP investigated by a terahertz scanning near-field optical microscope

Tinkara Troha, Arvind Singh , Petr Kužel , and Hynek Němec 

Institute of Physics of the Czech Academy of Sciences, Na Slovance 2, 18200 Prague, Czech Republic



(Received 22 January 2025; revised 29 May 2025; accepted 16 June 2025; published 8 July 2025)

Terahertz scanning near-field optical microscope (THz-SNOM) is employed to measure ultrafast evolution of terahertz conductivity spectra after photoexcitation of GaAs and InP wafers using ultrashort laser pulses. Unlike in GaAs, the terahertz photoconductivity decay in InP is controlled mainly by the diffusion of electrons away from the photoexcited area, and by the drift due to band bending at the surface of the semiconductor. We propose and discuss several general strategies of the analysis of signals measured using THz-SNOM, and we estimate the accuracy of the obtained near-field photoconductivity spectra.

DOI: [10.1103/x8m8-zgmw](https://doi.org/10.1103/x8m8-zgmw)

I. INTRODUCTION

Terahertz (THz) radiation is an efficient probe of charge transport mechanisms and properties in a large variety of materials, including classical semiconductors [1,2], semiconductor nanostructures [3], and carbon-based materials [3,4]. There are numerous advantages of using terahertz radiation: its strong interaction with free charges, the presence of characteristic spectral behavior due to carrier scattering rates falling into the terahertz spectral range, and the noncontact nature of the interaction, which eliminates the possible electrode effects. Experiments using time-domain terahertz spectroscopy can naturally incorporate an optical branch for sample photoexcitation: using the (time-resolved) optical pump–terahertz probe experiments, it is then possible to follow the photoinduced conductivity with subpicosecond time resolution [1,5].

Nowadays, relevant experimental methods as well as data analysis are well established for the case of conventional (far-field) transmission spectroscopy; however, its principal limitation in the context of nanostructures is the long wavelength of terahertz radiation ($1 \text{ THz} \triangleq 0.3 \text{ mm}$), which does not allow examination of individual deeply submillimeter objects due to the diffraction limit. This limit may be overcome using scanning near-field optical methods [6] or scanning tunneling microscopy [7]. Particularly useful is a technique based on the detection of the radiation scattered from an oscillating tip [scattering-type scanning near-field optical microscope (SNOM)]: thanks to the strong enhancement of the incident field at the nano-sized tip, the scattered radiation encodes information about the local properties of the sample in close vicinity of the tip apex [8,9]. It is thus possible to examine the conductivity or photoconductivity with submicron spatial resolution even in the terahertz range [10,11].

While the SNOM methods are frequently used for quantitative imaging without spectral resolution, the scattered broadband terahertz radiation contains in principle rich information about the local conductivity or permittivity spectra. The relation between the amplitude and phase of the scattered radiation and the sample properties is far from being simple

[9] and the models developed inevitably involve considerable simplifications regarding the tip, the sample, and their near-field interactions with the terahertz field. A point-dipole model [12] is the simplest model, which represents the tip as a finite-size sphere placed close to a half-space sample. The scattered signal is then considered to be proportional to the polarizability of the sphere/sample system. For a more quantitative analysis, the so-called finite-dipole model was developed, both for a bulk sample [13] and for layered systems [14]. This model approximates the tip as a finite conducting spheroid. In real materials, deciphering the sample properties can be considerably complicated by a possible spatial (time-dependent photo-) conductivity profile along the surface normal caused, for example, by a band bending and the consequent depletion or accumulation of charges close to the semiconductor surface [15].

In this paper, we theoretically analyze the outputs of THz-SNOM measurements in photoexcited semiconductors and the sensitivity of the experiments to important quantities such as the carrier concentration and the photoconductive layer thickness. We report on measurements of the ultrafast time evolution of photoinduced terahertz conductivity spectra in GaAs and InP. Both these materials with zinc-blende structure are usually considered as prototypical semiconductors with well-known properties, thus allowing us to verify our theoretical outcomes. Despite the apparent simplicity of the investigated samples, our study indicates that analysis of the THz-SNOM spectra brings complementary information to conventional far-field terahertz transmission spectroscopy such as information on the depth profile of the carrier concentration and its time evolution.

The paper is structured as follows. Parameters of the measurement setup and specifications of samples are introduced in Sec. II. In Sec. III, we thoroughly analyze the dependence of the scattered signal on relevant parameters, namely, on the photoexcited layer thickness and photocarrier density. We first identify the available measurable signals (Sec. III A) and, subsequently, we evaluate the sensitivity of these signals to the photoexcitation parameters (Sec. III B). In Sec. III C, we

examine how accurately the photocarrier density and photoexcited layer thickness can be retrieved from the measurable signals. In Sec. III D, we briefly discuss the frequency dependence of these results. In Sec. III E the detection by demodulation at higher harmonic frequencies of the tip tapping is analyzed. Experimental results for GaAs and InP are elaborated in Secs. IV and V, respectively. Finally, all the results are summarized in Sec. VI.

II. EXPERIMENT

The measurements are done with a scattering-type scanning near-field microscope (Neaspec) where a time-domain terahertz spectrometer operating in the spectral range between 0.5 and 2 THz is integrated into an atomic force microscope (AFM) device. The angle of incidence of p -polarized probing terahertz pulses is 60° . The AFM operates in the tapping mode; we use 40 nm platinum-iridium tips (Rocky Mountain Nanotechnology, 25PtIr200B-H40) driven at frequencies Ω_{tip} between 50 and 80 kHz. The tip-tapping amplitude was set to 150 nm and the minimum tip-sample distance was 1 nm. Femtosecond laser pulses (central wavelength 780 nm, maximum pulse energy 2 nJ, repetition rate 100 MHz, pulse duration 100 fs) synchronized in time with the probing terahertz pulses are used to photoexcite the sample. The scattered terahertz radiation is collected in a direction perpendicular to the incidence plane and at 60° with respect to the sample normal; the detected signal is demodulated at second through fifth harmonics of the tip-tapping frequency Ω_{tip} . The scattered terahertz spectra were measured as a function of the pump-probe delay. We verified that the scattered signal exhibited the expected translational symmetry scarcely disturbed by dust particles and ensured we measure the spectra in the homogeneous areas, far away from any perturbation (Fig. 15 in the Appendix).

The investigated (110) GaAs and (100) InP are standard high-resistivity commercial semi-insulating single crystal wafers with optically polished surfaces. The measurements are performed under a dry air atmosphere.

III. THEORY

A. Measurable signals

Here we will follow the finite-dipole model [13]. The scattered signal $s^{(m)}$ is assumed to be proportional to the effective tip polarizability $\alpha^{(m)}$ describing the near-field interaction between the tip and the sample, and to the far-field reflectance at the air-sample interface:

$$s^{(m)} \propto \alpha^{(m)}(1 + r)^2, \quad (1)$$

where m denotes the harmonics of the tip-tapping frequency (we concentrate on $m = 2$ and 3 , in our analysis). The expression for the effective polarizability of the tip in the vicinity of a layered structure was derived in [14]. The second term on the right-hand side accounts for the fact that the tip is illuminated both directly and by a beam reflected from the sample surface and that the scattered light propagates towards the detector both directly and after being reflected from the surface [13] (i.e., r is the terahertz far-field p -polarization reflectance of the sample at 60° incidence in our setup,

including interferences inside the photoexcited layer). Note that the quantities $s^{(m)}$, $\alpha^{(m)}$, and r , are generally frequency dependent (for the sake of the graphical clarity we omit marking this dependence in the formulas).

Altogether, Eq. (1) is a rather complex expression controlled not only by the response of the sample, but also by the tip geometry and settings of the SNOM (namely, by the tip radius, minimum tip-sample distance, and the tapping amplitude) and by semiempirical parameters (effective tip length L and the g factor, which is usually set to $0.7 e^{0.06i}$ according to the literature [13]).

Similarly to conventional spectroscopies, the detected signal depends on the intensity and shape of the incident pulse and on the instrumental response function. These are too difficult to evaluate, and it is thus necessary to establish a suitable reference. The standard possibility is normalization by the signal scattered from the unexcited sample; the analyzed scattered signal then reads

$$S^{(m)} \equiv \frac{s_{\text{exc}}^{(m)}}{s_{\text{gnd}}^{(m)}} = \frac{\alpha_{\text{exc}}^{(m)}}{\alpha_{\text{gnd}}^{(m)}} \frac{(1 + r_{\text{exc}})^2}{(1 + r_{\text{gnd}})^2} \equiv \alpha^{(m)} \frac{(1 + r_{\text{exc}})^2}{(1 + r_{\text{gnd}})^2}. \quad (2)$$

Here the subscript exc refers to the photoexcited sample and gnd to the unexcited sample (ground state), and $\alpha^{(m)}$ expresses the ratio of tip polarizabilities in the excited and ground states. With the scattering-type SNOM, it is possible to devise a self-referenced scheme, in which one analyzes the ratio of scattered signals belonging to different tip-tapping harmonics, m and m' , which is in fact equivalent to the ratio of the polarizabilities:

$$\frac{s_{\text{exc}}^{(m')}}{s_{\text{exc}}^{(m)}} = \frac{\alpha_{\text{exc}}^{(m')}}{\alpha_{\text{exc}}^{(m)}}. \quad (3)$$

The potential advantage of this approach is the elimination of the sample reflectance; such strategy could be particularly interesting for samples with complex surfaces where it may be difficult if not impossible to estimate the reflectance. On the other hand, any systematic error in the signal depending on the harmonics order would translate into a systematic error in the ratio (3). Such an issue should be eliminated upon normalization by appropriate ground-state signals:

$$X^{(mm')} = \frac{\frac{s_{\text{exc}}^{(m')}}{s_{\text{gnd}}^{(m')}}}{\frac{s_{\text{exc}}^{(m)}}{s_{\text{gnd}}^{(m)}}} = \frac{A^{(m')}}{A^{(m)}}. \quad (4)$$

This expression is independent of the sample reflectance, too.

B. Sensitivity study

We examine the sensitivity of these three approaches for the model case closely related to the experiments with the GaAs sample presented later in this paper. We consider that the sample consists of a homogeneous photoexcited layer with thickness d (Fig. 1) and properties of a high-resistivity GaAs excited at 780 nm (see the parameters in the caption of Fig. 2) on top of a semi-infinite unexcited substrate. The dielectric permittivity of the photoexcited sample (needed for the calculation of the SNOM response [13,14]) is modeled by

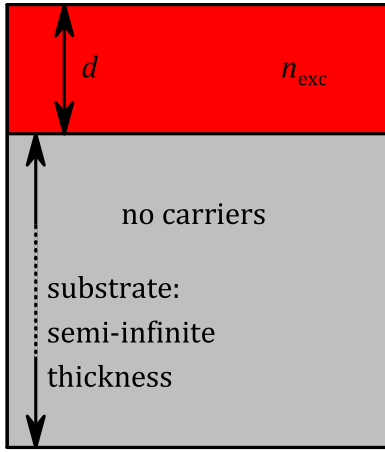


FIG. 1. Scheme of the model system investigated in Sec. III B and applicable also for the analysis of measurements in GaAs in Sec. IV.

the Drude formula:

$$\varepsilon_{\text{exc}} = \varepsilon_{\text{gnd}} - \underbrace{\frac{1}{2\pi i f \varepsilon_0} \frac{n_{\text{exc}} e_0^2}{m_{\text{eff}}} \frac{\tau}{1 - 2\pi i f \tau}}_{\Delta \varepsilon}, \quad (5)$$

where ε_{gnd} is the ground-state permittivity, ε_0 is the vacuum permittivity, $\Delta \varepsilon$ is the change of permittivity due to photoexcitation, f is the frequency of the terahertz light, n_{exc} is the density of photoexcited carriers, τ is their scattering time, and m_{eff} is their effective mass. For semiconductors, it is more natural to describe their photoinduced response in terms of their photoconductivity,

$$\Delta \sigma = -2\pi i f \varepsilon_0 \Delta \varepsilon, \quad (6)$$

or sheet photoconductivity,

$$\Delta \Sigma = d \Delta \sigma. \quad (7)$$

Since we encounter scattering times τ of about 150 fs and our central frequency f is about 1 THz, the term $2\pi f \tau$ in Eq. (5) is close to 1. In turn, our investigations are concentrated on the regime where the magnitudes of the real and imaginary parts of the photoconductivity are comparable to each other (the same holds for the photoinduced change in the permittivity).

In Fig. 2, we plot the scattered signal normalized by that from the unexcited sample [$S^{(2)}$, Eq. (2)] along with its decomposition into the individual terms (ratio of the tip polarizabilities $\alpha^{(2)}$ and ratio of far-field reflectances). We investigate the dependence on the carrier density and photoexcited layer thickness, which are two typical important parameters to be extracted from the measurements. While the most important dependence enters through the ratio of the tip polarizabilities $\alpha^{(2)}$ [Fig. 2(b)], the far-field reflectance term $(1 + r_{\text{exc}})^2 / (1 + r_{\text{gnd}})^2$ starts to play a considerable role for parameters corresponding to the upper right corner of Fig. 2(c), i.e., for the highest sheet conductivity values in the range presented in Fig. 2.

We represent the sensitivity of the measurement by the term $|S^{(m)} - 1|$, which corresponds to the relative change due to the photoexcitation, $||s_{\text{exc}}^{(m)} - s_{\text{gnd}}^{(m)}|/s_{\text{gnd}}^{(m)}|$; an analogic

expression, $|A^{(m)} - 1|$, is used to characterize the measurement sensitivity with respect to the near-field polarizability. The calculated data for the signal demodulated at $2\Omega_{\text{tip}}$ in our model GaAs sample is shown in Figs. 3(a) and 3(b). The contour lines show various levels of sensitivity in percents. Roughly, their shape between 3% and 30% can be approximated by an essentially vertical half line for thicker layers and a diagonal half line with a slope of -1 in the log-log scale for thinner layers. This approximation is indicated in Fig. 3(b) by the red dashed line for the sensitivity of 10%. The same trend is observed also for the normalized tip polarizability factor shown in Fig. 2(b) where both the vertical and diagonal parts are clearly apparent. From these simple comparisons of Figs. 2 and 3 it follows that up to about 30%, the sensitivity is controlled by the near-field polarizability, which provides here the main contribution to the signal. Figures 3(c) and 3(d) show the real part of conductivity and sheet conductivity within the explored space of parameters; the borders of the 10% sensitivity are plotted again as dashed lines. It follows that, in order to observe a 10% change in the signal, a minimum conductivity change of $\text{Re } \Delta \sigma \gtrsim 0.5 \text{ S/cm}$ and a minimum sheet conductivity change of $\text{Re } \Delta \Sigma \gtrsim 4 \mu\text{S}$ are required. The full diagonal line in Fig. 3(d) approximately indicates the onset of the far-field reflectance contribution to the signal ($\text{Re } \Delta \Sigma \gtrsim 1 \text{ m/S}$ in our model case).

C. Correlation of the retrieved parameters of photoexcited layer

Besides the sensitivity issues, the retrieval is complicated by the fact that the inverse mapping of the complex signal $S^{(m)}$ to n_{exc} and d might be ambiguous in some regions of the parameter space (n_{exc}, d) . To learn more about the inverse mapping, it is convenient to investigate the sensitivity of the retrieved values $(\ln n_{\text{exc}}, \ln d)$ on the complex signal $S^{(m)}$. In our model case, we assume that the absolute errors in the real (δS_{re}) and imaginary (δS_{im}) parts of the complex signal $S^{(m)}$ (or any other signal examined later in the paper) reach the same amplitude and that they are not correlated; the errors in $S^{(m)}$ are then represented by a circle with the radius given by the error amplitude $|\delta S|$ [Fig. 4(a)]. For reasonably small $|\delta S|$, linear expansion applies and the errors $\delta(\ln n_{\text{exc}})$ and $\delta(\ln d)$ (which are equivalent to the relative errors $\delta n_{\text{exc}}/n_{\text{exc}}$ and $\delta d/d$) can be expressed using the matrix transformation

$$\begin{pmatrix} \delta \ln n_{\text{exc}} \\ \delta \ln d \end{pmatrix} = \begin{pmatrix} n_{\text{exc}} \frac{\partial \text{Re} S}{\partial n_{\text{exc}}} & d \frac{\partial \text{Re} S}{\partial d} \\ n_{\text{exc}} \frac{\partial \text{Im} S}{\partial n_{\text{exc}}} & d \frac{\partial \text{Im} S}{\partial d} \end{pmatrix}^{-1} \begin{pmatrix} \delta S_{\text{re}} \\ \delta S_{\text{im}} \end{pmatrix}. \quad (8)$$

In general, the initial circle transforms into an inclined ellipse [Fig. 4(b)], called characteristic error ellipse in the following. The lengths of its semiaxes δa_{short} and δa_{long} are given by the following linear combinations:

$$\begin{aligned} \delta a_{\text{short}} &= \cos \theta \delta \ln n_{\text{exc}} + \sin \theta \delta \ln d \\ \delta a_{\text{long}} &= -\sin \theta \delta \ln n_{\text{exc}} + \cos \theta \delta \ln d, \end{aligned} \quad (9)$$

and they represent the errors in the determination of these linear combinations. It implies that the errors in the quantities $\ln n_{\text{exc}}$ and $\ln d$ are in general correlated and that the linear combination along the shorter semiaxis can be determined

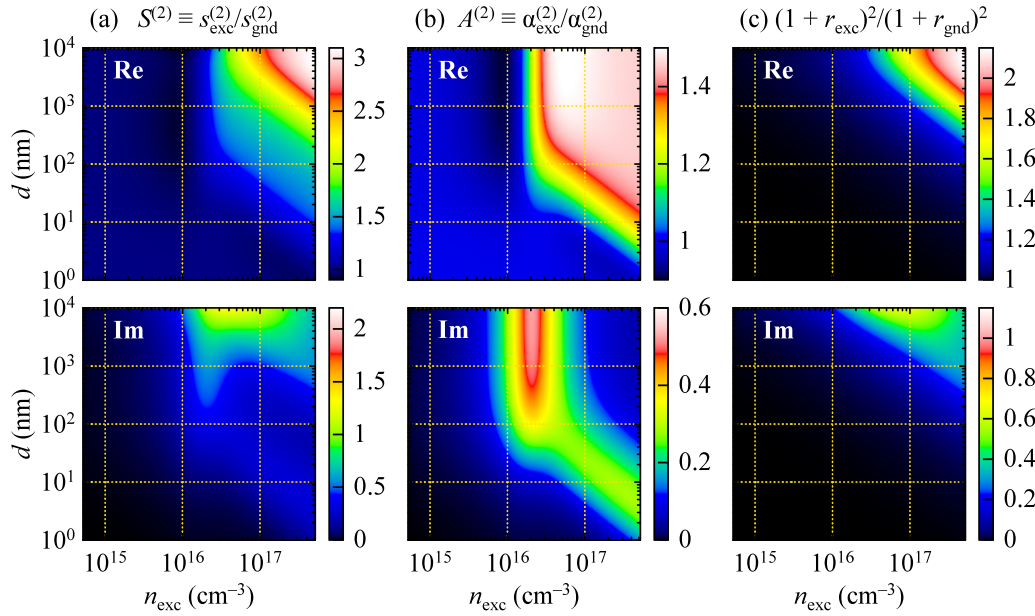


FIG. 2. (a) The ratio of the complex scattered signals in the excited and ground states demodulated at the second harmonics of the tip-tapping frequency and its decomposition into (b) the ratio of polarizabilities (near-field contribution) and (c) far-field reflectance contribution. Model parameters: $f = 1$ THz, tip-tapping amplitude $\Delta H = 150$ nm, tip radius $R = 40$ nm, effective tip length $L = 300$ nm, and $g = 0.7 e^{0.06i}$. Properties of GaAs: $\varepsilon_{\text{gnd}} = 13$, electron scattering time $\tau = 150$ fs, and electron effective mass $m_{\text{eff}} = 0.067m_e$.

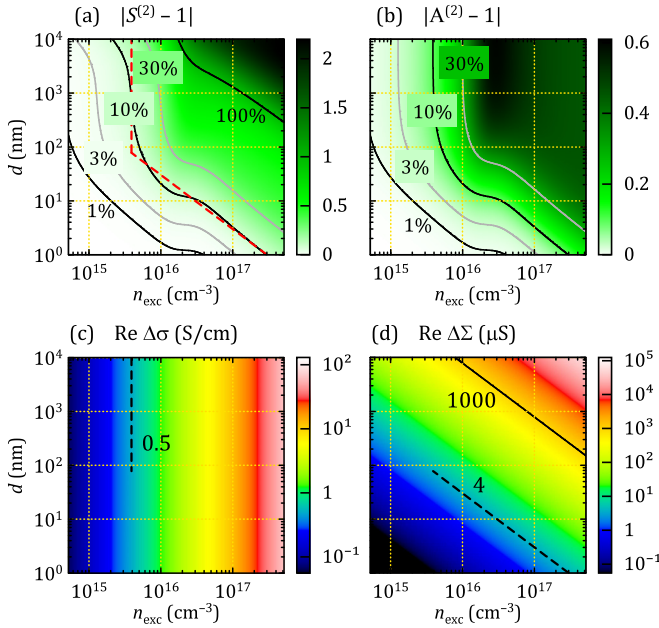


FIG. 3. (a), (b) Contour/colormap plots of the sensitivity of the signals (a) $|S^{(2)} - 1|$ and (b) $|A^{(2)} - 1|$ as a function of photocarrier concentration and film thickness. The red dashed line in (a) represents the approximation of the 10% sensitivity contour described in the text. (c), (d) Plots relating the sensitivity to the corresponding real (c) photoconductivity and (d) sheet photoconductivity of the photoexcited layer. The dashed lines correspond to the dashed segments in the plot (a) and express the minimum values of $\text{Re}\Delta\sigma \approx 0.5$ S/cm and $\text{Re}\Delta\Sigma \approx 4$ μS for achieving 10% sensitivity. The solid line ($\text{Re}\Delta\Sigma \approx 1$ mS) indicates the onset of the far-field reflectance contribution. A frequency of 1 THz is considered in all panels; model parameters are the same as in Fig. 2.

with a better accuracy than the linear combination along the longer semiaxis.

We applied this approach to our model photoexcited semiconductor layer and the results represented by δa_{short} and δa_{long} are shown in Fig. 5, together with the inclination of the ellipse given by the angle θ . Next, we discuss several important regions in the $(\ln n_{\text{exc}}, \ln d)$ space denoted by numbers ① – ③ in Fig. 5, where δa_{short} is quite small [dark-blue regions in Fig. 5(a)], i.e., where the resulting error might be reasonably small for one of the parameters $\ln n_{\text{exc}}$, $\ln d$, or for their appropriate linear combination. The marked regions do not have sharp and exact boundaries: the plotted dotted curves approximately indicate regions with some prominent properties.

In region ① the characteristic error ellipse is nearly vertical ($\theta \approx 0^\circ$) and reasonably narrow. Consequently, in this region, the carrier density can be determined accurately (5% error in the signal amplitude translates into less than 20% error in n_{exc}). However, δa_{long} acquires very high values (since

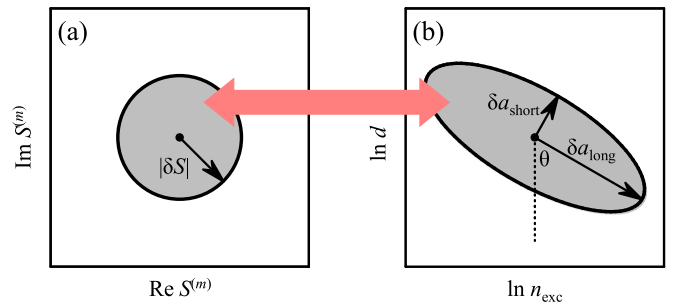


FIG. 4. Illustration of the inverse mapping of the measured signal ($\text{Re}S$, $\text{Im}S$) to the retrieved parameters $(\ln n_{\text{exc}}, \ln d)$.

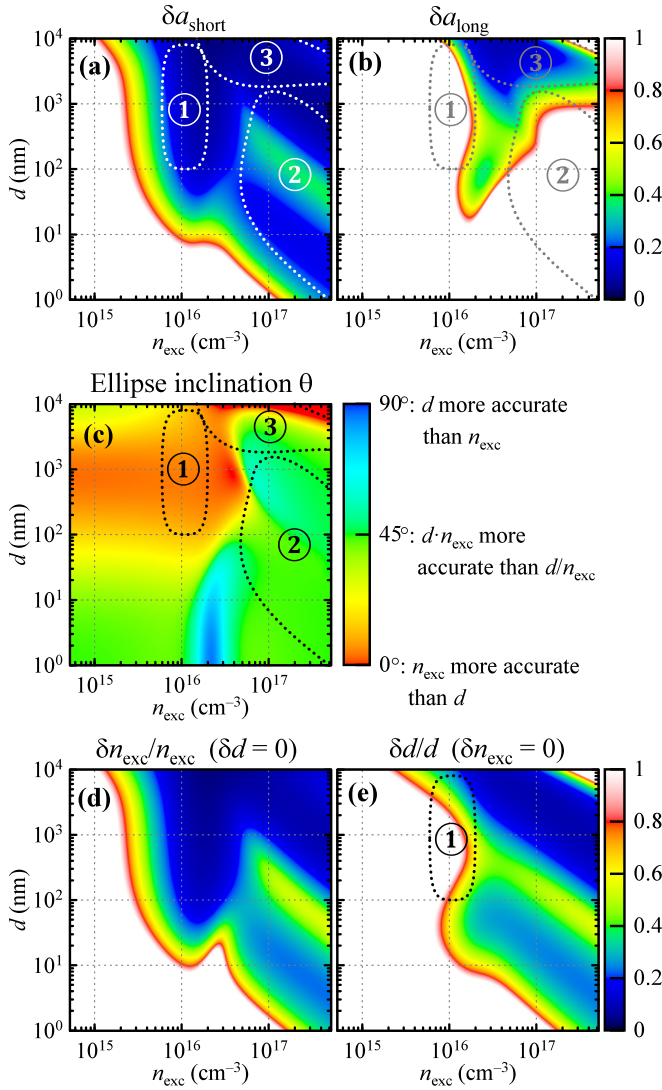


FIG. 5. (a), (b) Colormap plots of short (a) and long (b) axes of the error ellipse in the $(\ln n_{\text{exc}}, \ln d)$ space assuming the absolute error in the SNOM signal $S^{(2)}$ of $|\delta S^{(2)}| = 0.05$, which seems a reasonable estimate for a typical experiment. (c) Inclination of the error ellipse as defined in Fig. 4, and, in turn, also the correlation between the relative errors in n_{exc} and d ($\delta n_{\text{exc}}/n_{\text{exc}}$ and $\delta d/d$). (d), (e) Relative errors in n_{exc} and d calculated under an additional assumption that (d) d is *a priori* known ($\delta d = 0$) or (e) n_{exc} is *a priori* known ($\delta n_{\text{exc}} = 0$). In white regions the calculated error is 100% or larger. All the plots were calculated for the frequency of 1 THz. The numbered regions are described in detail in the text; they qualitatively indicate areas where some reasonable information on either excitation density or photoexcited layer thickness can be retrieved.

$|d\partial S^{(2)}/\partial d| \ll |n_{\text{exc}}\partial S^{(2)}/\partial n_{\text{exc}}|$; therefore, it is practically impossible to determine the photoexcited layer thickness.

In region ② the characteristic error ellipse is inclined by 45° counterclockwise indicating that the sum $\ln n_{\text{exc}} + \ln d$ (or, equivalently, the product $n_{\text{exc}}d$) can be retrieved reliably, while the difference $\ln n_{\text{exc}} - \ln d$ (or, equivalently, the ratio n_{exc}/d) cannot. Thus, this region can yield the sheet photoconductivity of the photoexcited layer, similarly as the conventional far-field terahertz transmission experiments on thin films.

Region ③ is characterized by the best sensitivity for an independent retrieval of n_{exc} and d . Note that this is the region where the reflectance term contributes significantly to the signal as observed in Fig. 2(c) and it thus seems that it is the interference in the thin photoexcited layer that is needed to facilitate the deconvolution of the carrier density and photoexcited layer thickness.

In comparison, we show in Fig. 5(d) the relative error in n_{exc} assuming that d is exactly known (e.g., the photoexcited layer thickness is determined independently from the absorption coefficient of the material at the excitation wavelength) and, similarly, in Fig. 5(e), we show the relative error in d assuming that n_{exc} is exactly known. The accessible regions of n_{exc} and d become significantly larger under these conditions and they both resemble the area of small values of δa_{short} depicted in Fig. 5(a) with the exception of region ① where the characteristic ellipse is nearly vertical and therefore d cannot be determined.

In brief, Figs. 5(a) and 5(c) together show that it is possible to retrieve either the conductivity or the sheet conductivity of the sample for a rather large space of parameters. Figure 5(b) then indicates the region where *both* n_{exc} and d can be retrieved with acceptable accuracy.

D. Frequency dependence

So far, we analyzed the signal behavior at the frequency of 1 THz. These conclusions can be easily generalized to an arbitrary frequency when the conductivity is dispersion free and the layer thickness is small. In such a case, the frequency and the carrier density controlling the scattered signal appear only in the form of the ratio n_{exc}/f in Eq. (5). Scaling the frequency and the carrier density by the same factor thus produces the same scattered signal. In other words, all patterns drawn in the $(\ln n_{\text{exc}}, \ln d)$ plane just shift in the $\ln n_{\text{exc}}$ direction upon scaling the frequency (as seen in Fig. 6). More importantly, it becomes obvious that the analysis of a broadband spectrum enhances the possibility of reaching a region with a good sensitivity and thus allows determination of the parameters by means of a frequency-dependent fit. These findings essentially underline the advantage in measuring the scattered signal in a broad spectral range.

In a general case, the frequency dependence is more complicated due to the dispersion of the conductivity described by the last (Drude) term in Eq. (5) for $2\pi f\tau \gtrsim 1$. Namely, the imaginary part of the conductivity exceeds the real part at high frequencies, which leads to an enhancement of the imaginary part of the signal $S^{(2)}$ as observed in Fig. 6 for 2 THz. Furthermore, for optically thicker photoexcited layers, interferences of the terahertz beam in the layer (which essentially depend on the product $n_{\text{exc}}f$) become important and further distort the pattern.

E. Notes on the signals at higher harmonics

A comparison of the ratios $S^{(m)}$ for the signal demodulation at different harmonics $m = 2, 3, 4$ shows qualitatively the same behavior for each m (Fig. 7). Quantitative changes are significant and can be visualized using contour lines. We observe a considerable vertical shift of the contour line in the

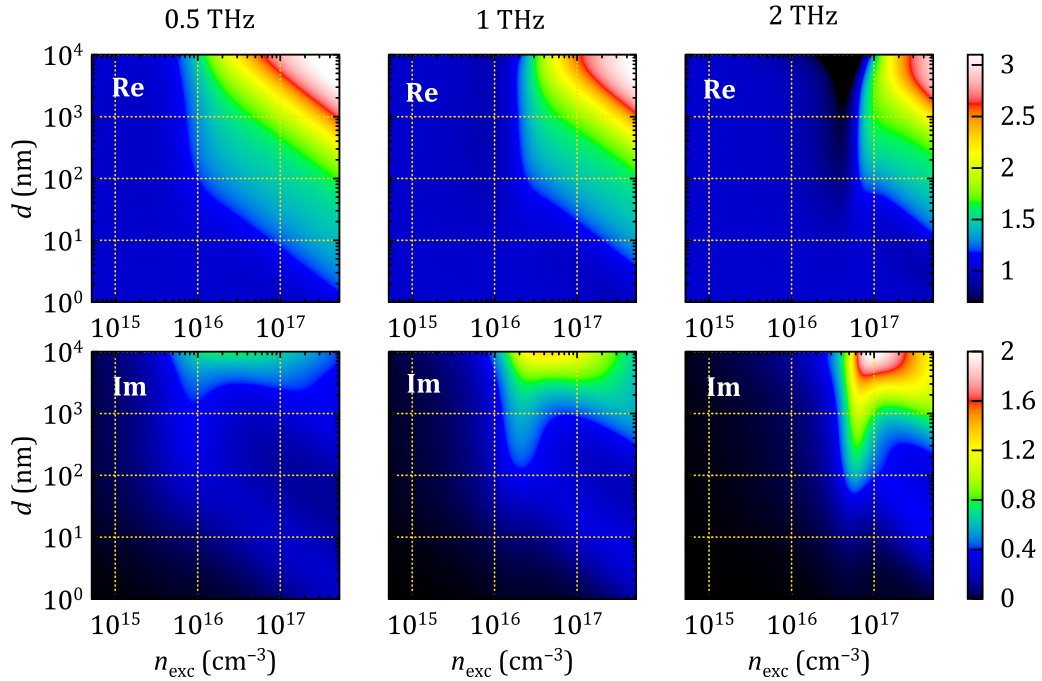


FIG. 6. Frequency dependence of the signal $S^{(2)} \equiv s_{\text{exc}}^{(2)}/s_{\text{gnd}}^{(2)}$. Model parameters are the same as in Fig. 2.

high-signal region, i.e., a shift towards a thinner photoexcited layer upon increasing the harmonic order. In other words, by using higher harmonics we reach a better sensitivity for thinner layers. Such a finding was recently pointed out in an experimental study of ultrafast carrier dynamics in GaAs nanobars [15]. Our current theoretical analysis thus further confirms the fact that a signal demodulated at higher harmonics comes from a thinner layer below the sample surface, and thus measurements using a set of harmonics in principle carry information about the depth profile of the photoconductivity.

Unlike the signal $S^{(2)}$ examined so far, the signal $X^{(2,3)}$ defined by Eq. (4) cancels the reflectivity including the interferences of the incoming and scattered beams in the photoexcited layer, and it is thus somewhat easier to interpret [see Figs. 8(a) and 8(b)]. Areas marked as ④ and ⑤ are interesting

since they approximately represent regions where the photoexcited layer thickness or the carrier density significantly alter the scattered signal. The signal in region ④ (photoexcited layer thickness exceeding ~ 50 nm) is controlled almost solely by the carrier density close to the surface whereas the signal in region ⑤ ($d \lesssim 50$ nm) is controlled almost solely by the sheet conductivity. It is thus the latter region in which the SNOM is selectively sensitive to what happens close to the tip, within the depth comparable with the tip radius. The drawback of this approach is a very limited sensitivity even in the “most promising” areas ④ and ⑤ [Figs. 8(c) and 8(d)]: a 5% noise in the measured signal $X^{(2,3)}$ translates into at least 40% error in the retrieved carrier density (region ④) and the sheet carrier density (region ⑤), which is ~ 4 times worse than for the signals $S^{(2)}$. The possibility to independently retrieve both the photoexcited layer thickness and the carrier concentration is rather theoretical; there is a very small gap between regions ④ and ⑤ where in the best case, both quantities can be obtained with approximately an order of magnitude accuracy. The reason is that the scattered intensities $s_{\text{exc}}^{(2)}$ and $s_{\text{exc}}^{(3)}$ depend on n_{exc} and d in rather similar ways: their ratio is thus almost constant and only the minor differences are available for the exploitation of information from the signal.

The character of the signal $s_{\text{exc}}^{(2)}/s_{\text{exc}}^{(3)}$ is almost identical to that of the signal $X^{(2,3)}$ (apart from the difference in the amplitudes) and the sensitivity to the errors is the same; for completeness, the plots are shown in the Appendix in Fig. 16. Due to the lack of any benefits, this strategy will not be used for the analysis of experimental data.

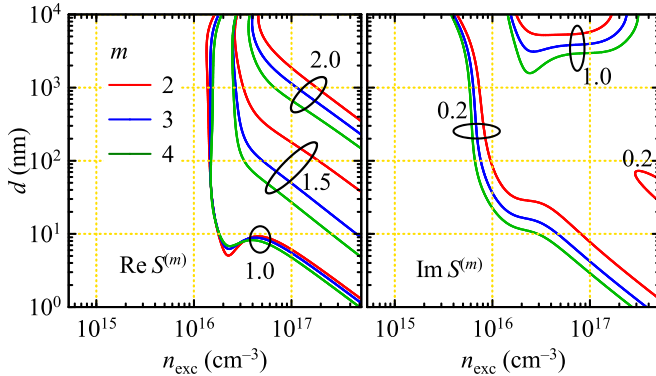


FIG. 7. Selected contour lines of the real and imaginary parts of the ratio $S^{(m)}$ at 1 THz for the demodulation at the second, third, and fourth harmonics of the tip-tapping frequency. The signal levels of $\text{Re}S^{(m)}$ and $\text{Im}S^{(m)}$ corresponding to the displayed contour lines are indicated close to the ellipses, which visually group contour lines with the same levels but different tip-tapping harmonics.

IV. EXPERIMENTAL RESULTS FOR GaAs

A. Signal $S^{(2)}$

The $S^{(2)}$ spectra measured on a bulk GaAs wafer (Fig. 9) exhibit a broad tip-plasmon resonance that redshifts as the

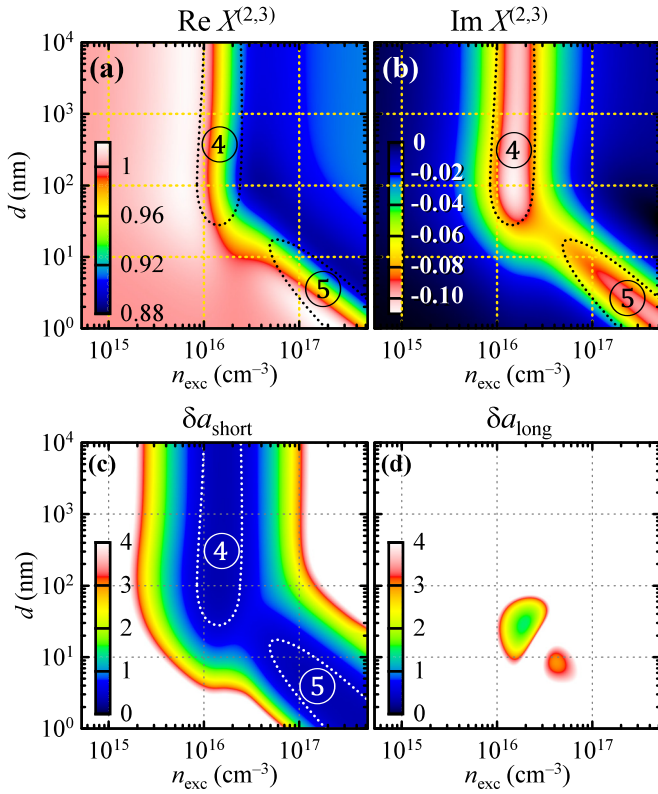


FIG. 8. (a), (b) Real and imaginary parts of the ratio of the complex scattered signal demodulated at the second and third harmonics, $X^{(2,3)}$. (c), (d) Colormap plots of short and long axes of the error ellipse in the $(\ln n_{\text{exc}}, \ln d)$ space assuming the absolute error in the signal $X^{(2,3)}$ of 0.05. Note that the color scale indicates much larger values than in Figs. 5(a) and 5(b). Similarly as in Fig. 4, the numbered regions qualitatively indicate areas where some reasonable information on either excitation density or photoexcited layer thickness can be retrieved.

density of photoexcited carriers decays with time after photoexcitation. Using far-field transient terahertz transmission spectroscopy, we verified that the lifetime of photoexcited charges in GaAs is subnanosecond (Fig. 17 in the Appendix), which implies that all photocarriers recombine before the next pump laser pulse impinges on the sample. Immediately after photoexcitation, the spatial carrier profile is thus a simple exponential with $1/e$ decay length of 750 nm in GaAs. Since the electron mobility in GaAs ($\sim 7000 \text{ cm}^2 \text{ V}^{-1} \text{ s}^{-1}$) is much higher than the hole mobility ($\sim 400 \text{ cm}^2 \text{ V}^{-1} \text{ s}^{-1}$), electrons rather than holes are probed.

For the analysis of the near-field interaction in GaAs, we approximate the photoexcited area by a layer with a (known) thickness of 750 nm with constant electron density, lying on an infinitely thick nonphotoexcited bulk (Fig. 1). The unknown material parameters are thus the free-electron density n_{exc} and the mean electron scattering time τ . There are also two semiempirical instrumental parameters introduced in [13]: the parameter g (set to $g = 0.7 e^{0.06i}$ according to [13]), and the effective tip length L (fitted, single value kept constant within each set of pump-probe delays).

The free-electron density decays exponentially with time [Fig. 10(a)]; practically the same evolution as well as

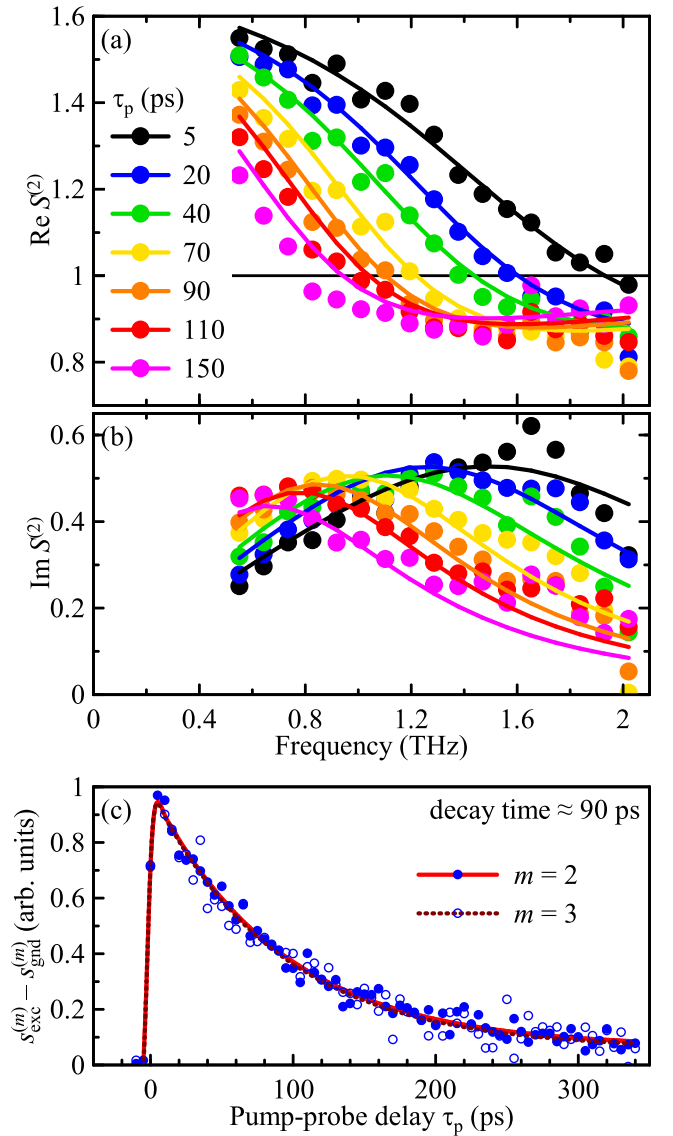


FIG. 9. (a), (b) The measured real and imaginary parts of the scattered SNOM signal at different times after photoexcitation τ_p normalized by the scattered signal from the unexcited sample [$S^{(2)}$, Eq. (5)] in GaAs. Points represent the experimental data; lines are obtained from the finite-dipole model fit. (c) Time evolution of the amplitude of the photoinduced changes of the scattered signals from photoexcited GaAs demodulated at the second and third harmonics of the tip-tapping frequency. Both signals are normalized to unity. Lines: fits by a monoexponential (decay time ≈ 90 ps) with a long-lived component.

absolute carrier density is deduced from signals demodulated at the second and third harmonics of the tip-tapping frequency. This is coherent with the assessed sensitivity [Fig. 5(d)]: the combination of a close-to-micron-thick photoexcited layer together with the observed carrier densities of 1×10^{16} to $5 \times 10^{16} \text{ cm}^{-3}$ falls just to the region where the carrier density can be determined with almost the best accuracy. The carrier density obtained from the measured data immediately after photoexcitation is $\sim 5.5 \times 10^{16} \text{ cm}^{-3}$.

The excitation pulse energy was 9 pJ and the excitation spot diameter visible on the camera in the SNOM $\sim 10 \mu\text{m}$

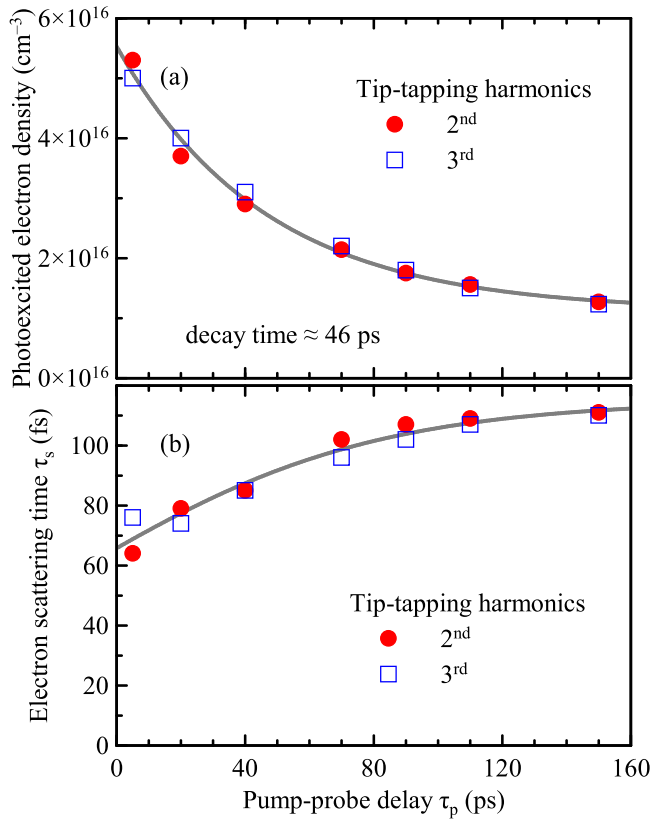


FIG. 10. Evolution of the fitted (a) concentration of electrons and (b) electron scattering time in photoexcited GaAs. The line in (a) is a fit by a monoexponential (decay time of ≈ 46 ps) with a long-lived component; the line in (b) serves to guide the eye only.

(Fig. 18 in the Appendix) implies an incident fluence of 4.6×10^{13} photons/ cm^2 . The excitation density can then be independently estimated: after accounting for the reflection losses on the semiconductor surface ($\sim 60\%$ for the employed s polarization and for the angle of incidence of the excitation beam of 60°) and assuming the penetration depth of 700 nm [16], we get $2.8 \times 10^{17} \text{ cm}^{-3}$, a 5 times larger value than that obtained from the fit. This density is an order of magnitude lower than the threshold for the absorption saturation for an 800-nm excitation wavelength [17].

It should be stressed that the excitation density is an order of magnitude estimate. Firstly, the determination of the excitation spot size is inaccurate since it is very small and there is no way how to resolve the actual beam profile at the sample surface; the visible spot borders may correspond to a rather arbitrary drop in the excitation intensity. Moreover, the excitation spot is rather inhomogeneous and currently we cannot control the exact positioning of the tip with respect to the spot and thus the actual sensed carrier density. Keeping in mind these issues, we consider the correspondence between the carrier density from the fit of the SNOM spectra and from the excitation fluence still acceptable.

The free-electron density [Fig. 10(a)] decays almost 2 times faster than the scattered SNOM signal at the maximum of the terahertz pulse [Fig. 9(c)], and the long-lived component is somewhat more pronounced. This emphasizes

a complex dependence of the scattered signal on the carrier density: although the raw evolution of the scattered signal is more easily measurable, an accurate assessment of the carrier dynamics generally requires a careful analysis of the spectra.

It is interesting that from the scattered SNOM signal it is possible to deduce also a more subtle effect: the evolution of the electron scattering time with carrier density [Fig. 10(b)]. These results are consistent with the carrier-density dependence of the electron mobility [18] (which is directly proportional to the electron scattering time τ_s) and which drops almost by a factor of 2 for densities reaching $5 \times 10^{16} \text{ cm}^{-3}$. Again, values retrieved from signals demodulated at the second and third harmonics are well consistent, mostly within 10% error.

The observed effect that the effective tip length depends on the harmonics of the tip-tapping frequency may seem somewhat puzzling: we obtained $0.87 \pm 0.07 \mu\text{m}$ for the second harmonics, and $1.9 \pm 0.3 \mu\text{m}$ for the third harmonics. Both values are considerably shorter than the real AFM tip length ($80 \mu\text{m}$). This indicates that one has to consider the effective tip length as an instrumental parameter with (so far) an unclear relation to the real geometry of the setup. Nevertheless, the consistency of the results retrieved from signals demodulated at different tip-tapping harmonics indicate that one can live with this approximation. We also realized that the effective tip length retrieved from repeated pump-probe experiments differs for different tips and setup adjustments, which suggests that it should be determined upon each change of the experimental setup.

Finally, note that the ambipolar diffusion length reaches 550 nm in 150 ps (for ambipolar diffusion coefficient $D_a = 20 \text{ cm}^2/\text{s}$, [19]) and it thus exceeds two-thirds of the initial excitation depth for the longest investigated pump-probe delays. We verified that assuming the photoexcited layer even as thick as 1000 nm affects the fitted material parameters by less than 5%, and it is thus possible to neglect the diffusion on this level of accuracy. This agrees with the results of the sensitivity study summarized in Fig. 5(c), which showed that the scattered SNOM signal is almost insensitive to the photoexcited layer thicknesses for the given experimental parameters.

B. Signal $X^{(2,3)}$

Measurement of the spectra $X^{(2,3)}$ is noisier, and the quality of the fit is much worse [Figs. 11(a) and 11(b)]. Despite that, both the value of the retrieved electron density and its evolution [Fig. 11(c)] match very well that found from the $S^{(2)}$ and $S^{(3)}$ spectra. Since the $X^{(2,3)}$ signal is insensitive to the layer thickness (Fig. 8), the photoexcited layer thickness was fixed to 750 nm in the fit; furthermore, the electron scattering time was fixed to 100 fs. For a good-quality fit, one needs to consider distinct effective tip lengths 0.7 and 1.4 μm for the signals demodulated at the second and third harmonics of the tip-tapping frequency, respectively. The difference from values obtained from $S^{(2)}$ and $S^{(3)}$ only underlines that this is an instrumental parameter so far.

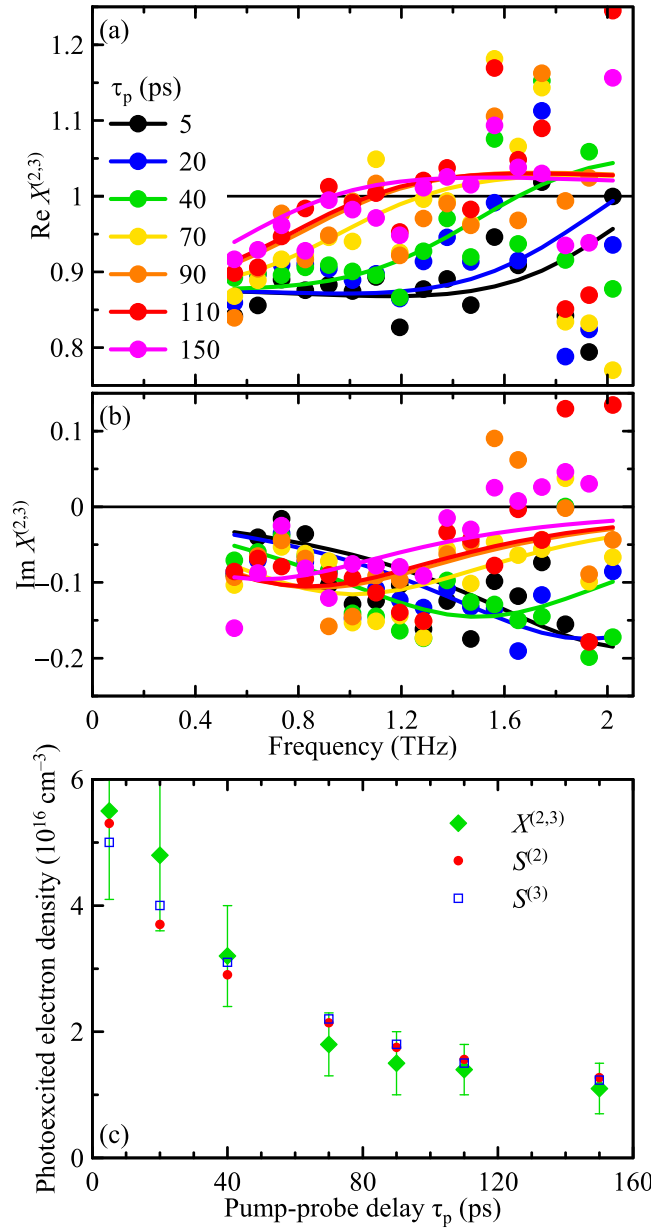


FIG. 11. (a), (b) The measured real and imaginary parts of the SNOM spectra $X^{(2,3)}$ at different times after photoexcitation τ_p in GaAs. Points represent the experimental data; lines are obtained from the finite-dipole model fit. (c) Evolution of the fitted concentration of electrons: comparison of results obtained from all three types of signals examined in the paper. Error bars for the $S^{(2)}$ and $S^{(3)}$ signals were omitted for graphical clarity: their standard deviation is $\leq 0.1 \times 10^{16} \text{ cm}^{-3}$.

V. EXPERIMENTAL RESULTS FOR InP – SIGNAL $S^{(2)}$

The SNOM spectra measured on bulk InP (Fig. 12) are at first glance similar to those in GaAs: a broad plasmon resonance redshifts as the density of photoexcited carriers decays with time after photoexcitation. The most prominent difference is the presence of the signal at a “negative” pump-probe delay, which in fact represents the state of the sample 10 ns after the arrival of the previous excitation pulse. When such long-lived electrons are present (see also Fig. 17 in the

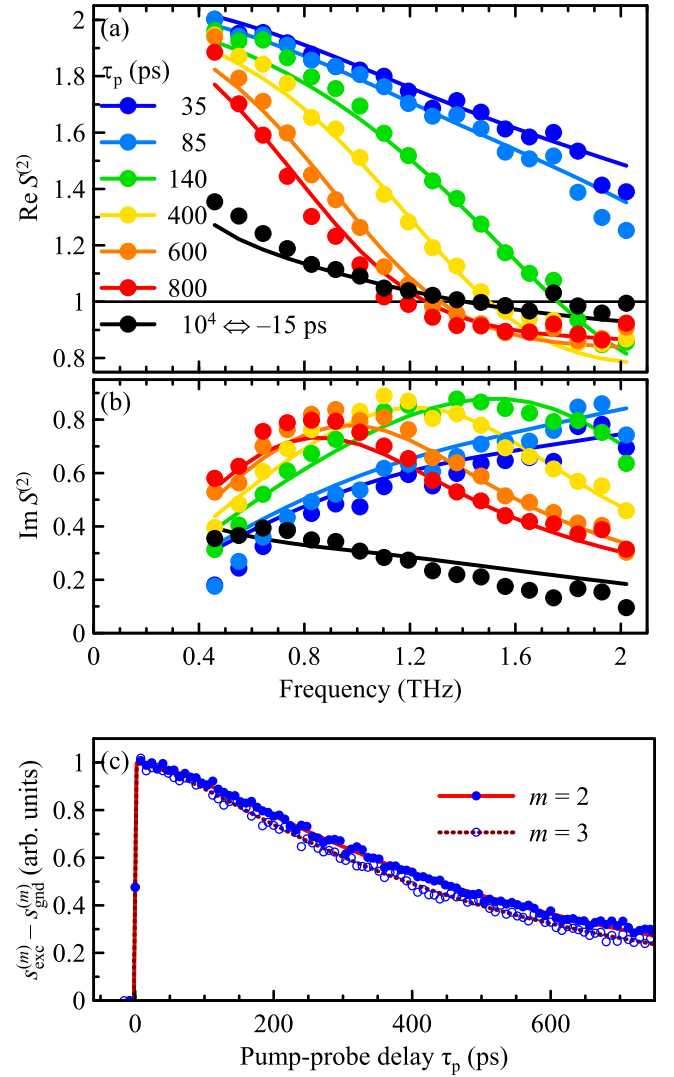


FIG. 12. (a), (b) The measured real and imaginary parts of the scattered SNOM signal normalized by that from the unexcited sample [Eq. (5)] at different times after photoexcitation τ_p in InP. Points represent the experimental data; lines are obtained from the finite-dipole model fit. (c) Time evolution of the amplitude of the photoinduced changes of the scattered signals from photoexcited InP demodulated at the second and third harmonics of the tip-tapping frequency. The signals are normalized to unity.

Appendix), one cannot neglect their redistribution in space due to the diffusion: The ambipolar diffusion coefficient of $10 \text{ cm}^2 \text{ s}^{-1}$ in InP [20] leads to the diffusion length of $3 \mu\text{m}$ during 10 ns in InP, which is an order of magnitude larger than the actual absorption depth of $\sim 350 \text{ nm}$ [16].

Furthermore, we observe that the decay of the $S^{(2)}$ signal [Fig. 12(c)] is significantly faster than the decay of the far-field transient transmittance (Fig. 14), which is proportional to the density of electrons integrated along the sample normal. This is strong evidence of a force pushing the electrons away from the surface, which is at the origin of the observed decrease of the scattered SNOM signal.

To model these two processes, we approximate the spatial distribution of free electrons using two layers (Fig. 13). The

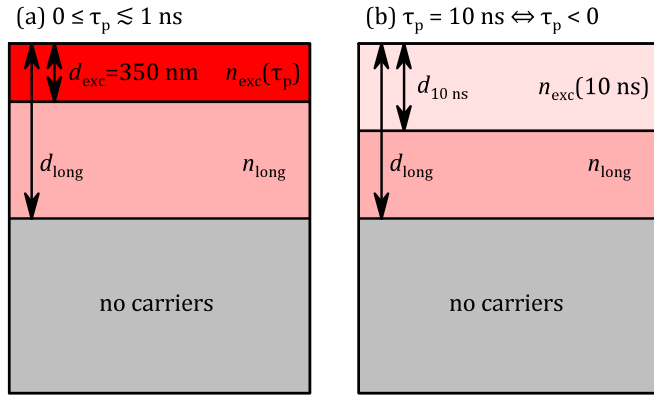


FIG. 13. Scheme of the carrier distribution in the model for calculating the SNOM response in InP.

top layer with the thickness d_{exc} contains a time-dependent free-electron density $n_{\text{exc}}(\tau_p)$: the layer thickness is set to the linear absorption depth in InP for pump-probe delays shorter than 1 ns [Fig. 13(a)], whereas it is allowed to expand to $d_{10 \text{ ns}}$ for the longest measured pump-probe delay (10 ns) [Fig. 13(b)]. The bottom layer reaches down to the time-independent depth d_{long} and we further consider that it contains a stationary free-electron density n_{long} .

The evolution of the electron density in the top layer (Fig. 14) obtained from the fit of the SNOM spectra shows faster dynamics than in GaAs, and considerably faster than the decay of the far-field signal representing the total electron density in the sample (including the charges in the deeper parts of the sample). This confirms the hypothesis that there is a driving force pushing electrons away from the surface: band bending is a typical effect responsible for this transport [15,21]. Dominance of surface recombination can be ruled out: it would also decrease the total density of electrons, which is not observed in the evolution of the far-field transient transmittance.

From the fits we found that the long-lived electrons spread down to $d_{\text{long}} = 6.0 \mu\text{m}$ away from the surface and that their density is $n_{\text{long}} = 3.3 \times 10^{16} \text{ cm}^{-3}$ (fit of the signal

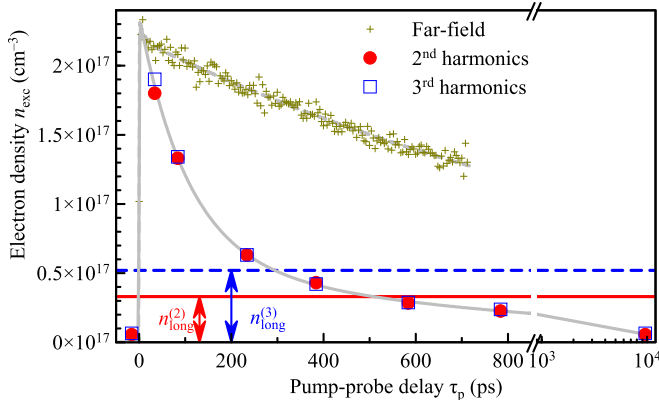


FIG. 14. Evolution of the retrieved concentration of electrons in photoexcited InP. The red and blue lines indicate the density of the long-lived charges as obtained from signals demodulated at second and third harmonics. The gray lines serve as a guide to the eye.

demodulated at the second harmonics of the tip-tapping frequency) or $n_{\text{long}} = 5.2 \times 10^{16} \text{ cm}^{-3}$ (fit of the third harmonics). At 600 ps after photoexcitation, the electron density in the top layer decays below that of the long-lived electrons deeper in the sample, and it further drops down to almost zero at 10 ns; at this pump-probe delay, the top layer thickness expands to $d_{10 \text{ ns}} = 1.4 \mu\text{m}$ (we found the same value from the fits of signals demodulated at the second and third harmonics). These findings manifest band bending close to the surface and therefore the presence of a force repelling electrons away from the surface [15]. Note also that the retrieved distances are close to the diameter of the excitation spot, which means that we are at the very limit where neglecting the lateral diffusion can be justified.

It is interesting to notice that here it was possible to independently retrieve both the carrier densities and the layer thicknesses with reasonable accuracy. This benefit may be understood within the sensitivity analysis performed for the single-layer system [Figs. 5(a) and 5(b)]: characteristic thicknesses around $6 \mu\text{m}$ and carrier densities on the level $3 \times 10^{16} \text{ cm}^{-3}$ fall right in the region where SNOM exhibits a rather good sensitivity to both quantities (mainly thanks to the surface reflectance). The density of the long-lived electrons n_{long} is the only parameter for which the fitting of the second and third harmonics yields somewhat different values. We attribute this discrepancy to the fact that the spatial density profile, upon the combined action of the diffusion and the repelling force, is rather complex and cannot be reproduced within the approximation of the applied model involving two layers with homogeneous carrier density.

The fitted effective tip length ($\sim 0.37 \mu\text{m}$ for both harmonics) differs from the value found when dealing with GaAs and thus only underlines the conclusion that it is an uncertain instrumental parameter on the current level of the description. The fitted initial carrier density is about 5 times lower than the estimate from the excitation fluence; this comparison is even better than for GaAs and the difference can be explained in an identical way.

GaAs and InP have the same crystallographic and similar electronic structures and the difference in THz-SNOM dynamics may thus seem confusing. The radiative recombination rates in intrinsic GaAs and InP ($7.21 \times 10^{-10} \text{ cm}^3/\text{s}$ and $1.26 \times 10^{-9} \text{ cm}^3/\text{s}$, respectively [22]) imply that in our experimental conditions (photocurrent concentrations of the order of $10^{16} - 10^{17} \text{ cm}^{-3}$) the bimolecular recombination would lead to a hyperbolic decay of the signal with time constants significantly exceeding the time interval between the pump pulses in the pulse train. This is not observed at least in GaAs. The lifetimes are thus likely to be controlled by unintentional doping, which might be very different for GaAs and InP. We verified that there are certain differences in the dynamics in (110) GaAs and (100) GaAs, but they are fundamentally smaller than those between GaAs and InP.

In this work, we focused mainly on the analysis of the spectra of the scattered signals and on their relation to the depth profile of the conductivity. The depth-profile sensitivity (apart from the obvious submicron spatial resolution) is an additional new feature compared to conventional far-field transient transmittance measurements. It should be noted that the depth also influences the dependence of the scattered

signal on the tip-tapping amplitude [11] and tip-tapping harmonics [15]. These are two further knobs that provide a piece of information on the conductivity depth profile. Nevertheless, further investigations are needed to explore the sensitivity and applicability limits of such approaches.

VI. SUMMARY

We analyzed theoretically the sensitivity of a THz-SNOM for the determination of the free-carrier density and thickness of the photoexcited layer with free carriers. The best measurable quantity for an independent determination of the carrier density and layer thickness is the ratio of the scattered signals from the excited and unexcited samples. The independent determination is possible for thicker layers thanks to the interferences of the incoming and scattered terahertz beam in the photoexcited layer. Analysis based on ratios of scattered signals at different tip-tapping harmonics is needed in the case of, e.g., a structured sample surface when it is impossible to account for the surface reflectance affecting the incoming and scattered terahertz beam; however, in this case the results are considerably less accurate and allow the retrieval of either the carrier density or the layer thickness, but not both at the same time.

The analysis of GaAs was rather straightforward thanks to its short lifetime, and in this sense, GaAs is indeed a prototypical semiconductor for SNOM pump-probe studies even with high laser repetition rates. In contrast, it turned out that InP requires a very careful interpretation of the spectra measured by the SNOM. The combination of a longer lifetime and band bending influences the carrier distribution over several microns and—due to the high laser repetition rate—thus affects the signal also at early times when a fresh laser pulse arrives. In our case, even these slow processes are directly seen in the spectra despite the fact that THz-SNOM is typically associated with a submicron spatial resolution.

The possible presence of band-bending effects is an obvious complication for interpreting the THz-SNOM spectra of semiconductors, which is only emphasized by the dependence of the degree of the band bending on the treatment of the surface. For example, we did not see any manifestation of band bending in GaAs in this work, while an extremely rapid escape of electrons from the surface was observed in the MBE-grown GaAs layer which, moreover, underwent nanofabrication [15]. On the other hand, the benefit of using SNOM compared to far-field transmission measurements is the certain degree of capability to probe and decode the depth profile of carrier density close to the surface.

ACKNOWLEDGMENTS

This work was supported by the Czech Science Foundation (Project No. 23-05640S). This work was also cofinanced by European Union and the Czech Ministry of Education, Youth and Sports (Project No. TERA-FIT-CZ.02.01.01/00/22_-008/0004594).

DATA AVAILABILITY

The data that support the findings of this article are openly available [23].

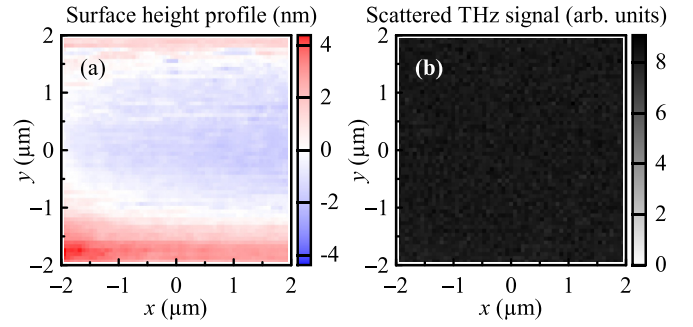


FIG. 15. Illustration of (a) height profile and (b) scattered terahertz signal (measured in the maximum of the terahertz wave form; demodulated at the second harmonics of the tip-tapping frequency) acquired from an area of $4 \times 4 \mu\text{m}^2$ selected on the investigated GaAs wafer. Both images confirm the homogeneous nature of the surface.

APPENDIX

The Appendix includes supplementary figures. Figure 15 confirms the homogeneity of the sample surface. In Fig. 16

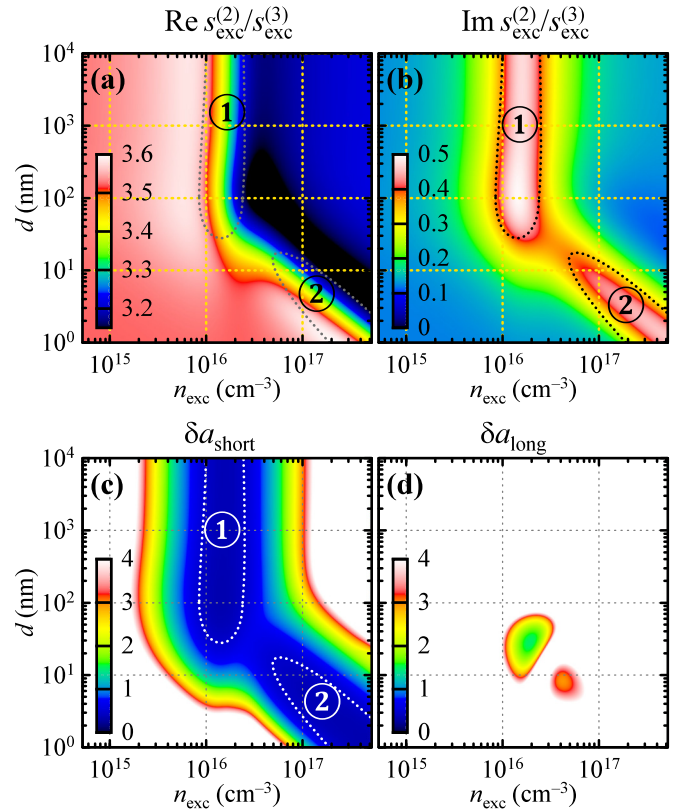


FIG. 16. (a), (b) Real and imaginary parts of the ratio of complex scattered signal demodulated at the second and third harmonics of the tip-tapping frequency, $s_{\text{exc}}^{(2)}/s_{\text{exc}}^{(3)}$. (c), (d) Colormap plots of short and long axes of the characteristic error ellipse in the $(\ln n_{\text{exc}}, \ln d)$ space assuming the relative error in the signal $s_{\text{exc}}^{(2)}/s_{\text{exc}}^{(3)}$ of 0.05. In the white regions the calculated error is 100% or larger. All the plots were calculated for the frequency of 1 THz and with the same model parameters as in Fig. 2.

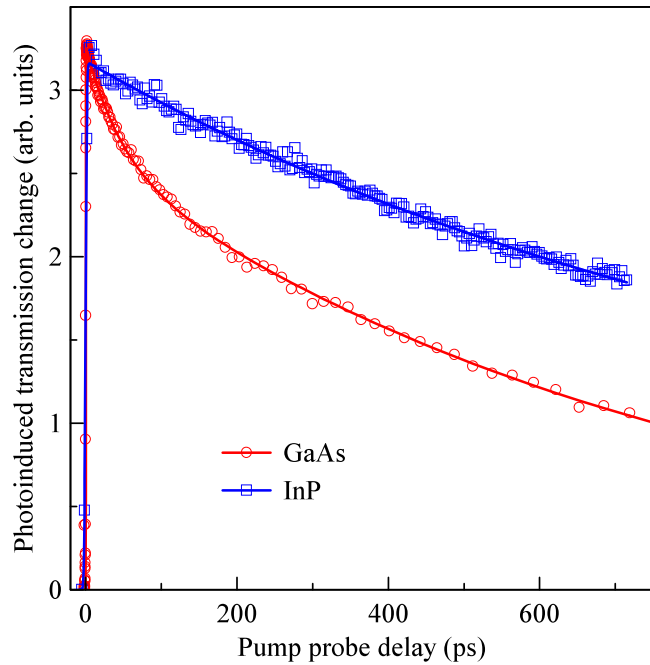


FIG. 17. Dynamics of the photoconductivity of the investigated GaAs and InP samples measured by a standard optical pump–THz probe spectroscopy in the far field. Symbols: measured data; lines: biexponential fits. Their parameters are 47 ps (80%) plus 790 ps (20%) for GaAs, and 990 ps (81%) plus the long-lived component (19%, its lifetime is at least several nanoseconds; a better estimate is not possible due to the limited time window of the measurement).

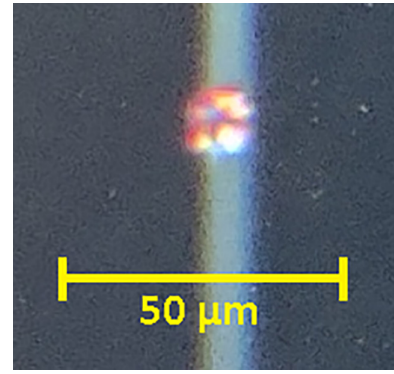


FIG. 18. Photo of the excitation spot (red) hitting a groove in a glass. The profile of the excitation intensity is clearly neither homogenous, nor Gaussian.

the ratio of scattered signals $s_{\text{exc}}^{(2)}/s_{\text{exc}}^{(3)}$ is shown, which complements Fig. 8 where the signals are normalized by their ground-state counterparts. Figure 17 shows the far-field dynamics which expresses the evolution of the free-carrier density integrated over entire thickness of the sample. Figure 18 is a photo of excitation spot which served for the estimation of the excitation density.

- [1] R. Ulbricht, E. Hendry, J. Shan, T. F. Heinz, and M. Bonn, Carrier dynamics in semiconductors studied with time-resolved terahertz spectroscopy, *Rev. Mod. Phys.* **83**, 543 (2011).
- [2] J. Lloyd-Hughes and T.-I. Jeon, A review of the terahertz conductivity of bulk and nano-materials, *J. Infrared Milli. Terahz. Waves* **33**, 871 (2012).
- [3] P. Kužel and H. Němec, Terahertz spectroscopy of nanomaterials: a close look at charge-carrier transport, *Adv. Opt. Mater.* **8**, 1900623 (2020).
- [4] C. J. Docherty and M. B. Johnston, Terahertz properties of graphene, *J. Infrared Milli. Terahz. Waves* **33**, 797 (2012).
- [5] C. A. Schmuttenmaer, Exploring dynamics in the far-infrared with terahertz spectroscopy, *Chem. Rev.* **104**, 1759 (2004).
- [6] T. L. Cocker, V. Jelic, R. Hillenbrand, and F. A. Hegmann, Nanoscale terahertz scanning probe microscopy, *Nat. Photon.* **15**, 558 (2021).
- [7] V. Jelic, S. Adams, M. Hassan, K. Cleland-Host, S. E. Ammerman, and T. L. Cocker, Atomic-scale terahertz time-domain spectroscopy, *Nat. Photon.* **18**, 898 (2024).
- [8] F. Zenhausern, M. P. O'Boyle, and H. K. Wickramasinghe, Apertureless near-field optical microscope, *Appl. Phys. Lett.* **65**, 1623 (1994).
- [9] F. Keilmann and R. Hillenbrand, Near-field microscopy by elastic light scattering from a tip, *Philos. Trans. R. Soc. A* **362**, 787 (2004).
- [10] A. J. Huber, F. Keilmann, J. Wittborn, J. Aizpurua, and R. Hillenbrand, Terahertz near-field nanoscopy of mobile carriers in single semiconductor nanodevices, *Nano Lett.* **8**, 3766 (2008).
- [11] M. Eisele, T. L. Cocker, M. A. Huber, M. Plankl, L. Viti, D. Ercolani, L. Sorba, M. S. Vitiello, and R. Huber, Ultrafast multi-terahertz nano-spectroscopy with sub-cycle temporal resolution, *Nat. Photon.* **8**, 841 (2014).
- [12] B. Knoll and F. Keilmann, Enhanced dielectric contrast in scattering-type scanning near-field optical microscopy, *Opt. Commun.* **182**, 321 (2000).
- [13] A. Cvitkovic, N. Ocelic, and R. Hillenbrand, Analytical model for quantitative prediction of material contrasts in scattering-type near-field optical microscopy, *Opt. Express* **15**, 8550 (2007).
- [14] B. Hauer, A. P. Engelhardt, and T. Taubner, Quasi-analytical model for scattering infrared near-field microscopy on layered systems, *Opt. Express* **20**, 13173 (2012).
- [15] V. Pushkarev, H. Němec, V. C. Paingad, J. Maňák, V. Jurka, V. Novák, T. Ostatnický, and P. Kužel, Charge transport in single-crystalline GaAs nanobars: Impact of band bending revealed by terahertz spectroscopy, *Adv. Funct. Mater.* **32**, 2107403 (2022).
- [16] D. E. Aspnes and A. A. Studna, Dielectric functions and optical parameters of Si, Ge, GaP, GaAs, GaSb, InP, InAs,

- and InSb from 1.5 to 6.0 eV, *Phys. Rev. B* **27**, 985 (1983).
- [17] F. Kadlec, H. Němec, and P. Kužel, Optical two-photon absorption in GaAs measured by optical-pump terahertz-probe spectroscopy, *Phys. Rev. B* **70**, 125205 (2004).
- [18] D. L. Rode and S. Knight, Electron transport in GaAs, *Phys. Rev. B* **3**, 2534 (1971).
- [19] B. A. Ruzicka, L. K. Werake, H. Samassekou, and H. Zhao, Ambipolar diffusion of photoexcited carriers in bulk GaAs, *Appl. Phys. Lett.* **97**, 262119 (2010).
- [20] Y. Song, L. Cao, B. D. Peng, G. Z. Song, Z. Q. Yue, J. M. Ma, L. Sheng, B. K. Li, and H. X. Wang, Investigation of an InP-based image converter with optical excitation, *Rev. Sci. Instrum.* **88**, 033109 (2017).
- [21] J. Lloyd-Hughes, S. K. E. Merchant, L. Sirbu, I. M. Tiginyanu, and M. B. Johnston, Terahertz photoconductivity of mobile electrons in nanoporous InP honeycombs, *Phys. Rev. B* **78**, 085320 (2008).
- [22] Y. P. Varshni, Band-to-band radiative recombination in groups IV, VI, and III-V semiconductors (I), *Phys. Status Solidi B* **19**, 459 (1967).
- [23] T. Troha, A. Singh, P. Kužel, and H. Němec, Dynamics of local photoconductivity in GaAs and InP investigated by THz SNOM [Dataset], doi:[10.57680/asep.0635607](https://doi.org/10.57680/asep.0635607).